Particle distribution function discontinuity-based kinetic immersed boundary method for Boltzmann equation and its applications to incompressible viscous flows

Ding Xu,[1,*] Yisu Huang,[1] and Jinglei Xu[2]

[1]*State Key Laboratory for Strength and Vibration of Mechanical Structures, Shaanxi Key Laboratory of Environment and Control for Flight Vehicle, School of Aerospace Engineering, Xi'an Jiaotong University, No. 28, Xianning West Road, Xi'an 710049, People's Republic of China*

[2]*School of Energy and Power Engineering, Beihang University, Beijing 100191, People's Republic of China*

(Received 10 September 2021; revised 28 December 2021; accepted 28 February 2022; published 28 March 2022)

In this paper, a general immersed boundary force density is introduced for the Boltzmann equation and finally expressed as the desired particle distribution function discontinuity across the immersed boundary. Because of its independence of any specific boundary conditions and any specific solvers for the Boltzmann equation, it actually establishes a unified framework to incorporate various types of boundary conditions and several different kinds of solvers for the Boltzmann equation. Hence, a particle distribution function discontinuity-based kinetic immersed boundary method (KIBM) for the Boltzmann equation is proposed based on this general immersed boundary force density. Subsequently, this paper primarily focuses on the isothermal incompressible fluid-solid flows, and uses the discrete unified gas kinetic scheme to solve the Boltzmann Bhatnagar-Gross-Krook model equation. Meanwhile, the regularized delta function and the bounce-back rule combined with an iterative IBM correction procedure are employed in obtaining the general immersed boundary force density to enforce the no-penetration and no-slip boundary conditions on the solid wall. Finally, some numerical experiments for typical incompressible fluid-solid flows show that the present KIBM could provide good agreement with other numerical and experimental results.

DOI: 10.1103/PhysRevE.105.035306

I. INTRODUCTION

The ability to simulate fluid flows with complex and moving boundaries accurately and efficiently has been an important issue in the computational fluid dynamics (CFD) community. Some conventional approaches based on a body-conforming grid algorithm generally are involved in a tedious grid generation procedure to tackle these fluid flows. In contrast, the immersed boundary method (IBM) can handle complex geometry with the use of the Cartesian grid, which can avoid many difficulties of grid generation encountered in conventional body-conforming discretizations. The idea of the original IBM was proposed by Peskin in the 1970s [1] to simulate blood flows in the heart. The novel feature of the IBM is that the physical boundary of the solid is treated as an infinitely thin shell with a set of Lagrangian points distributed on it, and the Navier-Stokes (NS) equations with a body force density are solved over the whole fluid domain represented by the surrounding Eulerian background points including both inside and outside of the solid body. The key issue in the IBM is how to effectively and efficiently determine the appropriate body force density for enforcing the no-slip and no-penetration boundary conditions on the body surface. According to the method of the body force density determination, the IBM is categorized into two approaches [2]. The first implementation, termed as the discrete forcing approach in the review article [2], introduces the forcing after the governing equations are discretized, so it depends on the specific discretization method. The numerical accuracy, stability, and other properties of the solver can be well controlled in this approach. Some important advantages of this approach are that the boundary can be retained as a sharp interface with no spreading and higher order local accuracy near the IB can be accomplished conveniently by adjusting the computational stencil near the IB [3–7]. However, for the moving boundary flows, the Lagrangian points usually are closely linked to the surrounding Eulerian background points and should be adjusted accordingly. Hence the algorithm is very complex, and the efficiency is reduced in this approach [8]. The second implementation, denoted as the continuous forcing approach in the review article [2], usually uses a weighting function to spread the force acting on the body surface, represented by a set of Lagrangian points, to the surrounding Eulerian background points. Because the Lagrangian points are defined independently of the Eulerian points in this approach, it is simple to implement and very attractive for complex flows with a moving boundary, such as many biological flows. The best-known way to compute restoring force is the penalty method [1], where a user-defined spring parameter is introduced. Recently, several extended and improved penalty IBM variations have been proposed for simulation of fluid–flexible body interaction problems in [9–11]. Another way is the direct forcing method first brought forward in [12]. Uhlmann [13] further proposed a new kind of direct forcing method where the forcing term is not obtained by any kind of feedback mechanism. Luo *et al.* [14] presented a multi-direct-forcing technique to enforce the no-slip and no-penetration boundary

*dingxu@mail.xjtu.edu.cn

conditions on body surface efficiently and accurately. Wu and Shu proposed a boundary-condition-enforced IBM based on the implicit velocity correction technique [15,16]. The relationships between the multi-direct-forcing IBM and the implicit velocity correction IBM were discussed in [17,18]. Recently, a general implicit direct forcing IBM was proposed for rigid particles of arbitrary shape and density [19]. Several different techniques for IBMs to enforce the no-slip boundary condition on body surface and accelerate iteration convergence were presented in [18,20,21]. Some excellent reviews about IBM may provide detailed information on this recent trend and applications [2,8,22–25].

On the other hand, we notice that the gas kinetic theory has received great attention in recent years to simulate fluid flows. The gas kinetic theory is a fluid flow description coming from a microscopic consideration, and the fundamental quantity in this microscopic description is the particle distribution function (PDF). The underlying flow dynamics described by the PDF is more fundamental and abundant than the macroscopic counterpart. The Boltzmann equation describing the evolution of the PDF is a well-established mathematical model of a fluid at microscopic level, and a variety of gas kinetic methods have been developed based on the Boltzmann equation, such as the lattice Boltzmann method (LBM) [26–28], gas kinetic scheme (GKS) [29,30], unified gas kinetic scheme (UGKS) [31,32], and discrete unified gas kinetic scheme (DUGKS) [33,34]. Indeed, these Boltzmann-based kinetic methods have demonstrated great potential as CFD tools offering some key advantages over the classical Navier-Stokes-based methods, and a variety of successful applications have been reported in Refs. [35–41]. Because both the IBM and LBM usually use the Cartesian grid, many researchers have combined them into a convenient and efficient method, denoted as IB-LBM. Feng and Michaelides [42] first adopted IB-LBM to numerically simulate the particulate flows. Other IB-LBMs based on different techniques, such as implicit velocity correction, momentum exchange, boundary thickening, and multi-direct-forcing, have been reported and widely applied to particulate flows, biological flows, and other fluid-solid interaction flows [15–18,37,43–46]. Peskin and Printz [47] and Lai and Li [48] pointed out that the governing equations of the IBM are mathematically equivalent to the conventional equations involving the jump condition for the fluid stress across the boundary. Recently, Suzuki *et al.* [49,50] proposed a stress tensor discontinuity-based IB-LBM. Yuan *et al.* attempted to combine IBM and GKS to simulate both incompressible and compressible viscous flows around stationary and moving rigid bodies [51,52]. Based on the Strang splitting algorithm, IB-DUGKS was reported in [53–55] to simulate particle-fluid flows and thermal convection flows. With the aid of the nonequilibrium extrapolation technique, Tao *et al.* proposed a novel PDF correction-based IB-DUGKS for fluid-particle flows [56].

In the IBM, the IB force density is a key factor introduced on the Lagrangian marker points to represent the fluid-solid interaction on the boundary. A lot of IBM variations have been proposed in the past decades to decide the IB force density for enforcing various types of boundary conditions on the surface of a body. However, these above studies usually adopted the constraint on macroscopic variables to determine the IB force density. Then different types of boundary conditions should be enforced for different macroscopic flow variables in different kinds of flows. This is a major drawback of the traditional IBMs.

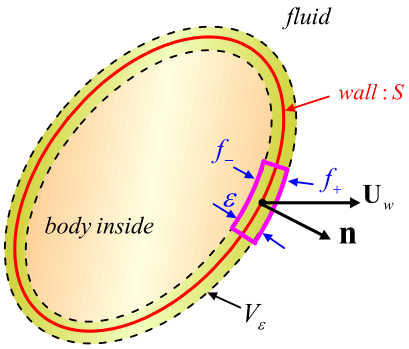

FIG. 1. A stationary or moving body immersed in fluid.

To the best of our knowledge, few studies have been published on the determination of IB force density based on the Boltzmann equation directly. Hence, this series of works will aim to propose a general IB force density based on the Boltzmann equation directly, and develop a unique kinetic immersed boundary method (KIBM). Some features and benefits of the present KIBM are summarized as follows. First, the general IB force density is expressed as the desired PDF discontinuity across the immersed boundary. Second, the general IB force density is independent of any specific boundary conditions and any specific solvers for the Boltzmann equation. Finally, the KIBM can incorporate various types of boundary conditions for different kinds of flows into a unified framework. In the current paper, we primarily focus on the isothermal incompressible fluid-solid flows, and use the discrete unified gas kinetic scheme (DUGKS) to solve the Boltzmann-BGK (Bhatnagar-Gross-Krook) model equation. Meanwhile, the bounce-back rule is employed in obtaining the desired PDF on both sides of the IB to enforce the no-penetration and no-slip boundary conditions on the solid wall. Further development of KIBM for thermal compressible flows will be presented in our subsequent work.

The organization of the rest of this paper is as follows. In Sec. II, we derive the general IB force density as the PDF discontinuity across the IB and discuss the property of the general IB force density. In Sec. III, we propose the KIBM based on the general IB force density and outline its implementation. In Sec. IV, we validate the present KIBM by several benchmark problems. Finally, conclusions and work in progress are reported in Sec. V.

II. GENERAL IMMERSED BOUNDARY FORCE DENSITY

A. Governing equations

A stationary or moving body immersed in a fluid is illustrated in Fig. 1. Let S be the body surface, and V be the domain including inside and outside of the body surface S. In the present kinetic immersed boundary method (KIBM), two sets of grids are used to represent the immersed boundary (IB) of the body and the background flow field, respectively. In accordance with practice, the IB is described by the Lagrangian

coordinate, and the background flow field is denoted by the Eulerian coordinate.

Here, the starting point is the Boltzmann's gas kinetic equation, including a general body force density, which can be expressed as

$$\frac{\partial f}{\partial t} + \mathbf{u}\cdot\nabla f = \Omega + G_E, \tag{1}$$

$$G_E(\mathbf{x},t) = \int_S G_L(\mathbf{X},t)\delta(\mathbf{x}-\mathbf{X})dS, \tag{2}$$

$$\frac{d\mathbf{X}}{dt} = \mathbf{U}(\mathbf{X},t) = \int_V \mathbf{U}(\mathbf{x},t)\delta(\mathbf{x}-\mathbf{X})d\mathbf{x}, \tag{3}$$

where $f = f(\mathbf{x},t,\mathbf{u})$ is the particle distribution function (PDF). $\mathbf{x}$, t, $\mathbf{u}$, and $G_E(\mathbf{x},t)$ are the Eulerian coordinate, time, particle velocity, and general body force density acting on the fluid, respectively. $\mathbf{X}$ and $G_L(\mathbf{X},t)$ stand for the Lagrangian coordinate and general IB force density. $\delta(\mathbf{x}) = \delta(x)\delta(y)\delta(z)$ is a three-dimensional Dirac delta function. Due to the mass and momentum conservation in particle collisions, the collision term Ω on the right side of Eq. (1) should satisfy the compatibility condition at any point in time and space,

$$\int \Omega\boldsymbol{\psi}d\Xi \equiv 0, \tag{4}$$

where $\boldsymbol{\psi} = (1,u,v,w)^T$ is the collision invariant, and $d\Xi = dudvdw$ is the volume element in the phase space. Let f^{eq} denote the Maxwellian equilibrium distribution function,

$$f^{eq} = \frac{\rho}{(2\pi RT)^{D/2}}\exp\left(-\frac{|\mathbf{u}-\mathbf{U}|^2}{2RT}\right), \tag{5}$$

where ρ is the fluid density, $\mathbf{U}$ is the macroscopic fluid velocity, T is the temperature, R is the gas constant, and D is the spatial dimension. The macroscopic conservative variables $\mathbf{Q}$ can be expressed as the moments of the distribution function,

$$\mathbf{Q} = (\rho,\rho u,\rho v,\rho w)^T = \int f^{eq}\boldsymbol{\psi}d\Xi = \int f\boldsymbol{\psi}d\Xi. \tag{6}$$

Equations (2) and (3) clearly represent the interaction between the body and fluid. Actually, the physical meaning of Eq. (3) is the no-slip and no-penetration boundary conditions satisfied on the body surface.

B. Formula of general immersed boundary force density $G_L(\mathbf{X},t)$

As is well known, the way to determine the IB force density is a key point in the IBM. In this paper, the general IB force density $G_L(\mathbf{X},t)$ is introduced in Eq. (2) and finally determined based on the Boltzmann equation directly.

In Fig. 1, the IB is treated as a shell V_ε with an infinitesimal thickness ε and enclosed by the surface S. A set of the Lagrangian marker points, independent of the background Eulerian grids for fluid flow, are distributed on the IB, and Eq. (1) is solved over the whole domain represented by the surrounding Eulerian background points including both inside and outside of the body.

When Eq. (1) is integrated over this shell V_ε, we obtain

$$\int_{V_\varepsilon}\frac{\partial f}{\partial t}d\mathbf{x} + \int_S f\mathbf{u}\cdot\mathbf{n}dS = \int_{V_\varepsilon}\Omega d\mathbf{x} + \int_S G_L(\mathbf{X},t)dS, \tag{7}$$

where $\mathbf{n}$ is the unit normal vector of the IB, pointing to the outside of the immersed body. Here, for the sake of simplicity, the fluid variables inside the body are marked with subscript "–" and outside the body are labeled "+". Let the shell thickness $\varepsilon \to 0$, so $G_L(\mathbf{X},t)$ can be obtained from Eq. (7),

$$G_L(\mathbf{X},t) = (f_+ - f_-)\mathbf{u}\cdot\mathbf{n} = [\![f]\!]\mathbf{u}\cdot\mathbf{n}. \tag{8}$$

Here, the square bracket $[\![\ ]\!]$ denotes a jump across the IB, and Eq. (8) clearly shows the relationship between the general IB force density $G_L(\mathbf{X},t)$ and the PDF discontinuity $[\![f]\!]$ across the IB.

It is noted that Eq. (8) is directly deduced from the Boltzmann's gas kinetic equation, so Eq. (8) is independent of any specific boundary conditions. In other words, Eq. (8) establishes a unified framework to handle various types of boundary conditions for different kinds of flows, which is a remarkable advantage compared to the traditional IBMs. In the meantime, Eq. (8) is independent of any specific solvers of the Boltzmann equation, so it can be flexibly combined with any solvers of the Boltzmann equation, such as LBM, DUGKS, and other discrete ordinate methods.

C. Moment of general IB force density $G_L(\mathbf{X},t)$

Here, let us further clarify the underlying physical meaning of the general IB force density $G_L(\mathbf{X},t)$ in Eq. (8).

Firstly, when Eq. (8) is integrated over the entire velocity space, one obtains the moment of $G_L(\mathbf{X},t)$,

$$\int G_L d\Xi = \int [\![f]\!]\mathbf{u}\cdot\mathbf{n}d\Xi = [\![\mathbf{U}]\!]\cdot\mathbf{n} = \mathbf{0}. \tag{9}$$

The deduction of Eq. (9) above utilizes the no-penetration boundary condition on the body surface. In the IBM, Eq. (9) also means that there is no mass exchange between the flows inside and outside of the body. Actually, besides the no-penetration boundary condition, the flows also satisfy the no-slip boundary condition on the body surface, so the velocity field is continuous across the IB,

$$[\![\mathbf{U}]\!] = \mathbf{0}. \tag{10}$$

Furthermore, when both sides of Eq. (8) are multiplied by particle velocity $\mathbf{u}$ and integrated over the entire velocity space, the first-order moment of $G_L(\mathbf{X},t)$ is obtained,

$$\begin{aligned}\mathbf{R} &= \int \mathbf{u}G_L d\Xi = \int [\![f]\!]\mathbf{u}\mathbf{u}\cdot\mathbf{n}d\Xi \\ &= -[\![\Sigma]\!]\cdot\mathbf{n} + \left(\mathbf{n} + \frac{\mathbf{U}\mathbf{U}\cdot\mathbf{n}}{RT}\right)[\![p]\!] \\ &\approx -[\![\Sigma]\!]\cdot\mathbf{n} + [\![p]\!]\mathbf{n} \quad \text{for incompressible flows.}\end{aligned} \tag{11}$$

The deduction of Eq. (11) utilizes the following fundamental formula describing the relationship between the PDF and stress tensor in the gas kinetic theory,

$$-p\mathbf{I} + \Sigma = -\int (\mathbf{u}-\mathbf{U})(\mathbf{u}-\mathbf{U})f d\Xi. \tag{12}$$

Here Σ is the viscous stress tensor, p is gas pressure, and $|\mathbf{U}|^2 \ll RT$ for incompressible flows. The first-order moment of $G_L(\mathbf{X},t)$, denoted as $\mathbf{R}$ here, is the boundary force density in the Navier-Stokes equation. The physical meaning of Eq. (11) is just the force balance equation of the Lagrangian

point $\mathbf{X}$ on the IB. With the consideration of the constitutive equation for incompressible Newtonian fluid flows,

$$\sum = 2\mu\mathbf{S}, \tag{13}$$

and the Caswell formula [57] for the strain-rate tensor $\mathbf{S}$ on a solid wall

$$2\mathbf{S} = \mathbf{n}[(\boldsymbol{\omega} - 2\boldsymbol{\omega}_b) \times \mathbf{n}] + [(\boldsymbol{\omega} - 2\boldsymbol{\omega}_b) \times \mathbf{n}]\mathbf{n}, \tag{14}$$

Equation (11) can be further simplified as follows for incompressible flows,

$$\begin{aligned}\mathbf{R} &= \int \mathbf{u} G_L d\Xi \\ &\approx -\mu[\![\boldsymbol{\omega}]\!] \times \mathbf{n} + [\![p]\!]\mathbf{n} \\ &= -[\![\boldsymbol{\tau}]\!] + [\![p]\!]\mathbf{n} \quad \text{for incompressible flows,}\end{aligned} \tag{15}$$

where $\boldsymbol{\omega}_b$ is the angular velocity of the body, $\boldsymbol{\omega} = \nabla \times \mathbf{V}$ is the vorticity, and $\boldsymbol{\tau} = \mu(\boldsymbol{\omega} - 2\boldsymbol{\omega}_b) \times \mathbf{n}$ is the skin-friction stress on the solid wall.

Subsequently, by taking the dot product of Eq. (15) with $\mathbf{n}$, one obtains

$$[\![p]\!] = \mathbf{R} \cdot \mathbf{n}, \tag{16}$$

which denotes the jump condition for pressure across the IB.

Finally, the jump condition for the skin-friction stress $\boldsymbol{\tau}$ across the IB is determined;

$$[\![\boldsymbol{\tau}]\!] = (\mathbf{R} \cdot \mathbf{n})\mathbf{n} - \mathbf{R}. \tag{17}$$

III. PARTICLE DISTRIBUTION FUNCTION DISCONTINUITY-BASED KINETIC IMMERSED BOUNDARY METHOD

A. Methodology

In Sec. II, the formula for the general IB force density $G_L(\mathbf{X}, t)$ has been obtained in Eq. (8). Now the general body force density $G_E(\mathbf{x}, t)$ in governing equation (1) could be accessed by spreading $G_L(\mathbf{X}, t)$ to the surrounding Eulerian grids according to Eq. (2):

$$G_E(\mathbf{x}, t) = \int_S G_L(\mathbf{X}, t)\delta(\mathbf{x} - \mathbf{X})dS = \int_S [\![f]\!](\mathbf{u} \cdot \mathbf{n})\delta(\mathbf{x} - \mathbf{X})dS. \tag{18}$$

Here $\delta(\mathbf{x}) = \delta(x)\delta(y)\delta(z)$ is a three-dimensional Dirac delta function. Since $G_L(\mathbf{X}, t)$ is integrated with a three-dimensional Dirac delta function over a two-dimensional surface S of the body, the resulting $G_E(\mathbf{x}, t)$ should be a one-dimensional singular Dirac delta function.

Afterward, the governing equation (1) will be handled by the operator splitting technique:

$$\begin{aligned}&\frac{\partial f}{\partial t} + \mathbf{u} \cdot \nabla f = \Omega + G_E(\mathbf{x}, t) \\ &\xrightarrow{\text{operator splitting}} \begin{cases}\text{DUGKS}: \frac{f^{(0)} - f^n}{\Delta t} + \mathbf{u} \cdot \nabla f = \Omega \\ \text{IBM correction}: \frac{f^{n+1} - f^{(0)}}{\Delta t} = G_E(\mathbf{x}, t)\end{cases}\end{aligned} \tag{19}$$

In this paper, we primarily focus on the isothermal incompressible fluid-solid flows, so the collision term Ω on the right side of Eq. (1) is replaced by the Bhatnagar-Gross-Krook (BGK) collision model. Due to the flexibility and stability of the DUGKS [33,58], the first step is numerically integrated by the DUGKS to obtain the intermediate PDF $f^{(0)}(\mathbf{x})$ without considering the effect of $G_E(\mathbf{x}, t)$. Subsequently, the IBM correction step will determine the desired PDF $f^{n+1}(\mathbf{x})$ which would satisfy the boundary conditions on the body surface:

$$\begin{aligned}f^{n+1}(\mathbf{x}) &= f^{(0)}(\mathbf{x}) + \Delta t G_E(\mathbf{x}, t) \\ &= f^{(0)}(\mathbf{x}) + \Delta t \int_S [\![f]\!](\mathbf{u} \cdot \mathbf{n})\delta(\mathbf{x} - \mathbf{X})dS.\end{aligned} \tag{20}$$

Here, the desired PDF $f^{n+1}(\mathbf{x})$ defined in the Eulerian grids is closely connected with the PDF discontinuity $[\![f]\!]$ across the IB, so the present IBM is named as the particle distribution function discontinuity-based kinetic immersed boundary method, which is abbreviated as KIBM for convenience in the following section.

B. Numerical implementation

In the actual numerical implementation, the singular Dirac delta function is approximately replaced by a smoothed regularized delta function D_n, which was proposed by Peskin [1,22],

$$D_n(\mathbf{x} - \mathbf{X}) = \begin{cases}\frac{1}{\Delta V_{E2}}\phi\left(\frac{x-X}{\Delta x}\right)\phi\left(\frac{y-Y}{\Delta y}\right), & n = 2: \text{ for 2D flows} \\ \frac{1}{\Delta V_{E3}}\phi\left(\frac{x-X}{\Delta x}\right)\phi\left(\frac{y-Y}{\Delta y}\right)\phi\left(\frac{z-Z}{\Delta z}\right), & n = 3: \text{ for 3D flows}\end{cases}, \tag{21}$$

$$\phi(r) = \begin{cases}\frac{1}{4}\left[1 + \cos\left(\frac{\pi|r|}{2}\right)\right], & |r| \leqslant 2 \\ 0, & |r| > 2\end{cases}, \tag{22}$$

where $\Delta V_{E2} = \Delta x \Delta y = \Delta x^2$ and $\Delta V_{E3} = \Delta x \Delta y \Delta z = \Delta x^3$ are the corresponding volume of the Eulerian grid for two-dimensional (2D) and three-dimensional (3D) flows, respectively. The Eulerian grids near the IB should be uniform $\Delta x = \Delta y = \Delta z$. With the aid of Eq. (21), now Eq. (20) can be rewritten as follows,

$$f^{n+1}(\mathbf{x}) = f^{(0)}(\mathbf{x}) + \Delta t \sum_{\mathbf{X} \in \mathbf{L}} [\![f]\!](\mathbf{u} \cdot \mathbf{n}) D_n(\mathbf{x} - \mathbf{X})\Delta S_L, \tag{23}$$

where ΔS_L is the arc length of the IB element for 2D flows, or the area of the IB element for 3D flows, respectively.

Because the singular Dirac delta function $\delta(\mathbf{x} - \mathbf{X})$ is approximately replaced by the smoothed regularized delta function $D_n(\mathbf{x} - \mathbf{X})$, the no-slip and no-penetration boundary conditions would be satisfied approximately on the body surface. As a result, the unphysical streamline penetration phenomenon would emerge on the IB, which would destroy the mass conservation. Just as in the multi-direct-forcing method proposed by Luo *et al.* [14], here an iterative IBM correction procedure is adopted to avoid the above deficiency. Then the governing equation (1) is handled by the operator splitting technique with multiple IBM correction

steps,

$$\frac{\partial f}{\partial t}+\mathbf{u}\cdot\nabla f=\Omega+G_E(\mathbf{x},t)=\Omega+\sum_m G_E^{(m)}=\Omega+G_E^{(1)}+G_E^{(2)}+\cdots+G_E^{(m)}+\cdots$$

$$\xrightarrow{\text{operator splitting}}\begin{cases}\text{DUGKS}: & \frac{f^{(0)}-f^n}{\Delta t}+\mathbf{u}\cdot\nabla f=\Omega\\ \text{first IBM correction}: & \frac{f^{(1)}-f^{(0)}}{\Delta t}=G_E^{(1)}\\ \text{second IBM correction}: & \frac{f^{(2)}-f^{(1)}}{\Delta t}=G_E^{(2)}\\ \cdots & \\ m\text{th IBM correction}: & \frac{f^{(m)}-f^{(m-1)}}{\Delta t}=G_E^{(m)}\end{cases}. \tag{24}$$

Hence $f^{(m)}(\mathbf{x})$ can be obtained as follows,

$$\begin{aligned}f^{(m)}(\mathbf{x})&=f^{(m-1)}(\mathbf{x})+\Delta t G_E^{(m)}(\mathbf{x})\\&=f^{(m-1)}(\mathbf{x})+\Delta t\sum_{\mathbf{X}\in\mathbf{L}}[\![f^{(m-1)}(\mathbf{X})]\!](\mathbf{u}\cdot\mathbf{n})D_n(\mathbf{x}-\mathbf{X})\Delta S_L,\end{aligned} \tag{25}$$

where $f^{(m-1)}(\mathbf{x})$ is the intermediate PDF, and $f^{(m-1)}(\mathbf{X})$ can be interpolated from $f^{(m-1)}(\mathbf{x})$ by the smoothed regularized delta function D_n:

$$f^{(m-1)}(\mathbf{X})=\sum_{\mathbf{x}\in\mathbf{E}}f^{(m-1)}(\mathbf{x})D_n(\mathbf{x}-\mathbf{X})\Delta V_E. \tag{26}$$

In this paper, the isothermal incompressible fluid flows are primarily focused on, and the no-penetration and no-slip boundary conditions should be satisfied on the wall for the macroscopic fluid velocity. Hence, the bounce-back (BB) rule [59] is used to determine the desired f_+ and f_- on both sides of the IB as follows:

$$f_+^{(m-1)}(\mathbf{X},\mathbf{u})=\begin{cases}f^{(m-1)}(\mathbf{X},-\mathbf{u})+2\rho_+W_i\frac{\mathbf{u}\cdot\mathbf{U}_w}{RT}, & \mathbf{u}\cdot\mathbf{n}>0\\ f^{(m-1)}(\mathbf{X},\mathbf{u}), & \mathbf{u}\cdot\mathbf{n}\leqslant 0\end{cases}, \tag{27}$$

$$f_-^{(m-1)}(\mathbf{X},\mathbf{u})=\begin{cases}f^{(m-1)}(\mathbf{X},-\mathbf{u})+2\rho_-W_i\frac{\mathbf{u}\cdot\mathbf{U}_w}{RT}, & \mathbf{u}\cdot\mathbf{n}<0\\ f^{(m-1)}(\mathbf{X},\mathbf{u}), & \mathbf{u}\cdot\mathbf{n}\geqslant 0\end{cases}. \tag{28}$$

Here $\mathbf{n}$ is the unit normal vector of the IB, pointing to the outside of the immersed body. $\mathbf{u}$ is the discrete particle velocity and W_i is the associated weight. $\mathbf{U}_w$ is the wall velocity. ρ_+ and ρ_- are the densities on both sides of the IB determined by the definition of the wall density as follows:

$$\rho_+=\left[\sum_{\mathbf{u}\cdot\mathbf{n}=0}f^{(m-1)}(\mathbf{X},\mathbf{u})+2\sum_{\mathbf{u}\cdot\mathbf{n}<0}f^{(m-1)}(\mathbf{X},\mathbf{u})\right]\Bigg/\left(1-\frac{2}{RT}\sum_{\mathbf{u}\cdot\mathbf{n}>0}W_i\mathbf{u}\cdot\mathbf{U}_w\right), \tag{29}$$

$$\rho_-=\left[\sum_{\mathbf{u}\cdot\mathbf{n}=0}f^{(m-1)}(\mathbf{X},\mathbf{u})+2\sum_{\mathbf{u}\cdot\mathbf{n}>0}f^{(m-1)}(\mathbf{X},\mathbf{u})\right]\Bigg/\left(1-\frac{2}{RT}\sum_{\mathbf{u}\cdot\mathbf{n}<0}W_i\mathbf{u}\cdot\mathbf{U}_w\right). \tag{30}$$

Finally, within N_{IBM} times of IBM correction, the desired PDF $f^{n+1}(\mathbf{x})$ satisfying the boundary conditions can be well approached by $f^{(N_{\text{IBM}})}(\mathbf{x})$:

$$f^{n+1}(\mathbf{x})=f^{(N_{\text{IBM}})}(\mathbf{x}). \tag{31}$$

In summary, the update of the distribution function f from t_n to t_{n+1} in the present KIBM can be outlined as follows:

(1) Compute the intermediate PDF $f^{(0)}(\mathbf{x})$ from $f^n(\mathbf{x})$ by DUGKS.

(2) for $(m=1; m\leqslant N_{\text{IBM}}; m++)$.

(a) Obtain $f^{(m-1)}(\mathbf{X})$ from $f^{(m-1)}(\mathbf{x})$ by Eq. (26).

(b) Calculate $f_+^{(m-1)}(\mathbf{X},\mathbf{u})$ and $f_-^{(m-1)}(\mathbf{X},\mathbf{u})$ using Eqs. (27) and (28).

(c) Obtain the general IB force density $G_L^{(m)}(\mathbf{X},t)=[\![f^{(m-1)}]\!]\mathbf{u}\cdot\mathbf{n}$ as in Eq. (8).

(d) Spread $G_L^{(m)}(\mathbf{X},t)$ to $G_E^{(m)}(\mathbf{x},t)$ by Eq. (18).

(e) Update $f^{(m)}(\mathbf{x})$ by Eq. (25).

(3) According to Eq. (31), obtain the desired PDF $f^{n+1}(\mathbf{x},t)$ satisfying the boundary conditions.

(4) Set $n=n+1$, repeat steps (1)–(3) until convergence is reached.

It is noted that the Peskin's isotropic regularized delta function is used in this paper, such as in Eq. (26), so the present KIBM should be categorized into the diffusive interface IBM, although the PDF discontinuity $[\![f]\!]$ across the IB is sharply determined by the multi-direct-forcing method.

C. Other technical details for the completeness of the algorithm

1. Determination of the Lagrangian element thickness ε

The quantities φ in the transformation step between the Lagrangian and Eulerian locations can be written as follows

[13],

$$\mathbf{E} \to \mathbf{L}: \quad \varphi(\mathbf{X}) = \sum_{\mathbf{x}\in\mathbf{E}} \varphi(\mathbf{x}) D_n(\mathbf{x}-\mathbf{X}) \Delta V_E, \tag{32}$$

$$\mathbf{L} \to \mathbf{E}: \quad \varphi(\mathbf{x}) = \sum_{\mathbf{X}\in\mathbf{L}} \varphi(\mathbf{X}) D_n(\mathbf{x}-\mathbf{X}) \Delta V_L, \tag{33}$$

where $\Delta V_E = \Delta x \Delta y \Delta z$ and $\Delta V_L = \varepsilon \cdot \Delta S_L$ are the volume of the Eulerian and Lagrangian grids, respectively. ΔS_L is the arc length of the IB element for 2D flows, or the area of the IB element for 3D flows, respectively. Theoretically, the IB thickness ε would approach zero. However, in the actual implementation, due to the finite scale of both the Lagrangian and Eulerian grids, ε cannot be infinitesimal. The value of ε is really significant for the spreading procedure $\mathbf{L} \to \mathbf{E}$ in the IBM as in Eq. (33). Thus one question is how to decide the value of ε.

At the beginning of the present work, ε was empirically estimated as follows,

$$\varepsilon_1 \approx \Delta x, \tag{34}$$

where Δx is the size of the corresponding Eulerian grid around the IB. This approach has been widely utilized in the IBMs [13,45,60].

In the next moment, we evaluated the IB thickness ε based on some physical considerations. Firstly, it is found that both $G_E(\mathbf{x}, t)$ and the collision term Ω are on the right side of Eq. (1), so $G_E(\mathbf{x}, t)$ would represent some collision mechanism to enforce the no-slip and no-penetration boundary conditions. Furthermore, recalling the formula $G_L(\mathbf{X}, t) = [\![f]\!]\mathbf{u} \cdot \mathbf{n}$ from Eq. (8), we hypothesized that the particles on both sides of the IB move toward the IB, travel for a time step, and then collide on the IB. On the macroscopic scale, the accumulation effect of these particle collisions is just to enforce the no-slip and no-penetration boundary conditions on the body surface. Hence the IB thickness ε is evaluated as follows:

$$\varepsilon_2 \approx (\bar{u}_{\rm rms} - U_{w,n})\Delta t + (\bar{u}_{\rm rms} + U_{w,n})\Delta t = 2\bar{u}_{\rm rms}\Delta t, \tag{35}$$

where $\bar{u}_{\rm rms} = \sqrt{3RT}$ is the root mean square (rms) thermal speed and $U_{w,n}$ is the wall velocity along the body surface normal direction.

Combing Eq. (34) with Eq. (35), one obtains

$$\varepsilon_2/\varepsilon_1 \sim \bar{u}_{\rm rms}\Delta t/\Delta x \sim CFL \sim O(1). \tag{36}$$

The CFL number in the DUGKS [33,34] usually is less than 1.0 for numerical stability, so these two approaches would give similar results. In the actual implementation, both of the above two approaches work well in the following studies.

2. Evaluation of force and torque acting on the body

As shown in Fig. 1, the mass of the IB shell can be ignored when the shell thickness $\varepsilon \to 0$, so all forces acting on the IB shell would be in balance, which has been shown in Eq. (11). Now, the force $\mathbf{F}(t)$ and torque $\mathbf{T}(t)$ acting on the body can be evaluated as follows:

$$\begin{aligned}\mathbf{F}(t) &= \int_S (\textstyle\sum_+ \cdot \mathbf{n} - p_+\mathbf{n}) dS \\ &= \mathbf{F}_{\rm in}(t) - \int_S \mathbf{R} dS \\ &= \mathbf{F}_{\rm in}(t) - \sum_{m=1}^{N_{\rm IBM}} \sum_{\mathbf{X}\in\mathbf{L}} \left(\Delta S_L \int \mathbf{u} G_L^{(m)} d\Xi \right),\end{aligned} \tag{37}$$

$$\begin{aligned}\mathbf{T}(t) &= \int_S (\mathbf{X} - \mathbf{X}_c) \times (\textstyle\sum_+ \cdot \mathbf{n} - p_+\mathbf{n}) dS \\ &= \mathbf{T}_{\rm in}(t) - \int_S (\mathbf{X} - \mathbf{X}_c) \times \mathbf{R} dS \\ &= \mathbf{T}_{\rm in}(t) - \sum_{m=1}^{N_{\rm IBM}} \sum_{\mathbf{X}\in\mathbf{L}} \left(\Delta S_L (\mathbf{X} - \mathbf{X}_c) \times \int \mathbf{u} G_L^{(m)} d\Xi \right).\end{aligned} \tag{38}$$

Here $\mathbf{X}_c$ is the coordinate of the center of mass. $\mathbf{F}_{\rm in}(t) = \int_S (\textstyle\sum_- \cdot \mathbf{n} - p_-\mathbf{n}) dS$ and $\mathbf{T}_{\rm in}(t) = \int_S (\mathbf{X} - \mathbf{X}_c) \times (\textstyle\sum_- \cdot \mathbf{n} - p_-\mathbf{n}) dS$ are the force and torque acting on the virtual fluid inside of the body; they usually are called the internal mass effect and can be approximately evaluated by several approaches [19,45,61]. In the present work, the rigid body approximation of Feng and Michaelides [61] is used to evaluate the internal mass effect $\mathbf{F}_{\rm in}(t)$ and $\mathbf{T}_{\rm in}(t)$,

$$\mathbf{F}_{\rm in}(t) \approx \frac{\rho_f}{\rho_b} M \frac{\mathbf{U}_c(t) - \mathbf{U}_c(t-\Delta t)}{\Delta t}, \tag{39}$$

$$\mathbf{T}_{\rm in}(t) \approx \frac{\rho_f}{\rho_b} I_b \frac{\boldsymbol{\omega}_b(t) - \boldsymbol{\omega}_b(t-\Delta t)}{\Delta t}, \tag{40}$$

where ρ_f, ρ_b, M, $\mathbf{U}_c$, I_b, and $\boldsymbol{\omega}_b$ are fluid density, body density, the mass of the body, the velocity of the mass center of the body, the momentum of inertia, and the angular velocity of the body, respectively.

IV. NUMERICAL RESULTS

In this section, the present KIBM is validated by several benchmark problems including the stationary body, prescribed moving body, and freely moving body flows. For all cases in this work, the local Ma number is always less than 0.3, so the flows could be considered as incompressible. For the boundary conditions, the bounce-back rule [59] is used for the straight wall boundary, while the nonequilibrium extrapolation method [62] is used for the open boundary. The number of IBM corrections $N_{\rm IBM}$, unless otherwise stated, is set as $N_{\rm IBM} = 20$. In the actual implementation, the size of the Lagrangian grid ΔS_L has the same order as the Eulerian grid size Δx in order to avoid the unphysical leakage [22]. Similar to the original DUGKS [33], the Gauss-Hermite quadrature is employed to discretize the particle velocity space in the present KIBM. For one-dimensional flows ($D = 1$), the discrete velocities and associated weights are

$$u_{\pm 1} = \pm\sqrt{3RT}, \quad u_0 = 0, \quad W_{\pm 1} = 1/6, \quad W_0 = 2/3. \tag{41}$$

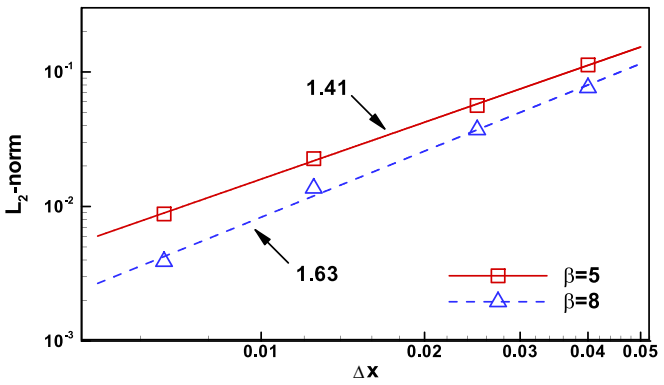

FIG. 2. Spatial convergence of the present KIBM in the cylindrical Couette flow.

For higher-dimensional flows ($D > 1$), the tensor product method is used to generate the discrete velocities and associated weights.

A. Accuracy verification of the present kinetic IBM

The original DUGKS method has been numerically proved to be a fully second-order scheme in some recent studies [33,63]. After combining with the present KIBM, it is necessary to discuss the accuracy of the whole flow solver. Hence, the accuracy of the present KIBM will be verified by the cylindrical Couette flow, which is widely chosen as a benchmark problem for the IBM accuracy test [53,64].

In this cylindrical Couette flow problem, the fluid flow is confined by two coaxial rotating cylinders. Usually, the governing equation for this flow is written in the cylindrical polar coordinate as

$$\frac{d^2U_\theta}{dr^2} + \frac{d}{dr}\left(\frac{U_\theta}{r}\right) = 0, \tag{42}$$

with the corresponding boundary conditions

$$U_\theta|_{r=R_1} = U_1 = \omega_1 R_1, \quad U_\theta|_{r=R_2} = U_2 = \omega_2 R_2, \tag{43}$$

where R_1, R_2 and ω_1, ω_2 are the radius and angular speed of the inner and outer rotating cylinders, respectively. U_θ is the circumferential velocity component. The steady solution

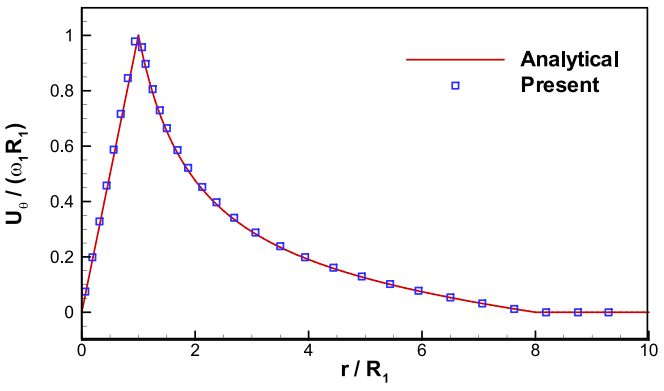

FIG. 3. Velocity profile for the cylindrical Couette flow.

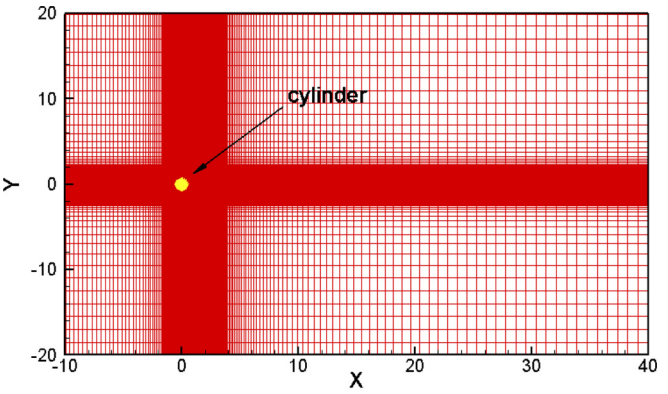

(a) Global view of grid

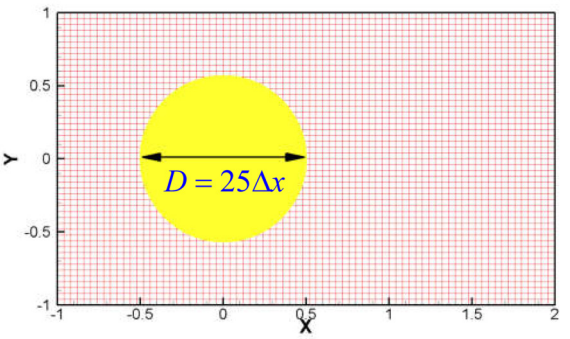

(b) Zoom-in view around the cylinder

FIG. 4. Nonuniform grid (221 × 149) for 2D flow around a stationary circular cylinder.

of this flow can be obtained as follows:

$$U_\theta = C_1 r + \frac{C_2}{r}, \quad C_1 = \frac{\omega_2 R_2^2 - \omega_1 R_1^2}{R_2^2 - R_1^2},$$
$$C_2 = \frac{(\omega_1 - \omega_2) R_1^2 R_2^2}{R_2^2 - R_1^2}. \tag{44}$$

In the simulation, the outer cylinder is fixed ($\omega_2 = 0$). CFL = 0.5, the Mach number $\mathrm{Ma} = U_1/\sqrt{\gamma RT} = 0.1$, the Reynolds number $\mathrm{Re} = U_1(R_2 - R_1)/\nu = 20$, and two different values of radius ratio $\beta = R_2/R_1$ are set as $\beta = 5, 8$. Here ν is the kinematic viscosity of fluid.

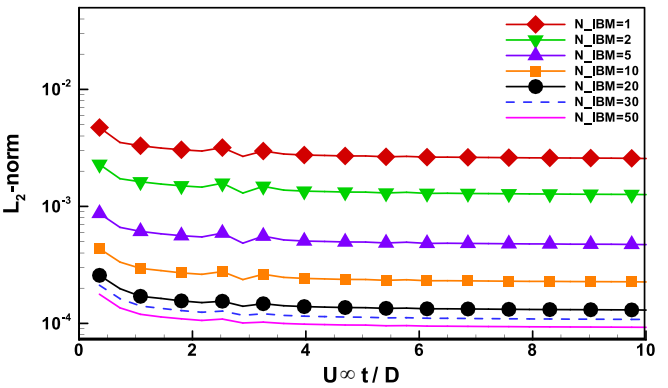

FIG. 5. Time history of the $L2$-norm error of velocity with different values of N_{IBM}.

TABLE I. The performance overhead of KIBM on numerically simulating the flow around a stationary circular cylinder at Re = 20.

Grid	Minimum	Eulerian	Lagrangian		Time cost for 1000 steps (s)					
					Present			Tao's IBM [56]		
No.	grid size	Grids	Grids	N_{IBM}	DUGKS	IBM	Ratio	DUGKS	IBM	Ratio
Grid 1	$\Delta x = D/25$	221 × 149	80	1	189.6	11.1	0.06	196.5	11.0	0.06
				10	191.1	111.4	0.58	196.6	109.3	0.56
				20	196.9	227.5	1.16	198.0	218.1	1.10
Grid 2	$\Delta x = D/40$	281 × 209	200	1	353.8	20.5	0.06	364.8	20.2	0.06
				10	365.5	212.1	0.58	364.5	202.0	0.55
				20	355.9	410.0	1.15	365.3	405.0	1.11

Usually, the numerical error L_2-norm is used to evaluate the accuracy of the scheme, and L_2-norm is defined as

$$L_2-\text{norm} = \sqrt{\frac{1}{N}\sum_{i=1}^{N}[|\mathbf{U}_i - \mathbf{U}_e|^2]}, \tag{45}$$

where $\mathbf{U}_i$ is the numerical solution, and $\mathbf{U}_e$ is the analytical solution in Eq. (44). N is the total number of Eulerian grids locating between the inner and outer cylinders. Four grids with different spacing Δx are chosen to obtain the corresponding numerical error L_2-norm; they are shown in Fig. 2. It is observed that the slopes of these lines are about 1.4–1.6. As a result, it can be concluded that the present KIBM has first-order accuracy in space, which is comparable with other diffusive interface IBMs [53,65]. In the meantime, the comparison between the analytical solution and the numerical solution by the present KIBM is shown in Fig. 3 for the case $\beta = 8$, which clearly shows that the present results have good agreements with the analytical solution.

B. Flow around a stationary circular cylinder

The flow around a stationary circular cylinder is a classical fluid dynamics problem. There are abundant numerical and experimental results for this flow in the literature. Moreover, this problem has been widely chosen to investigate whether the no-slip and no-penetration boundary conditions are satisfied in the IBM variations [13–15,43,53]. This flow is controlled by the Reynolds number $\mathrm{Re} = U_\infty D/\nu$. Here, U_∞, D, and ν are the free stream velocity, the cylinder diameter, and the kinematic viscosity, respectively.

It is well known that the long history of the flow field is a steady flow when Re is less than about 47. Hence, the influence of IBM correction times N_{IBM} on the satisfaction of the no-slip and no-penetration boundary conditions is investigated at Re = 20. In the simulation, CFL = 0.5 and the computational domain is set by a square domain ($L \times W = 50D \times 40D$) with a nonuniform grid (221 × 149), which is shown in Fig. 4. The region near the cylinder adopted a refined uniform grid with size $\Delta x = D/25$. Eighty Lagrangian points are uniformly distributed along the cylinder surface, so the ratio of the Lagrangian grid size to Eulerian grid size is about $\Delta S_L/\Delta x = 0.982$. The free-stream Mach number is set to be 0.1. A nonequilibrium extrapolation method is used for all the boundary conditions, while the velocity at the inlet boundary is fixed and the pressure at the outlet boundary is fixed. Here the L_2-norm error of velocity on the cylinder boundary is presented in Fig. 5 with different values of N_{IBM}. It is clear that L_2-norm declines as N_{IBM} increases, so the no-slip and no-penetration boundary conditions can be enforced in the present KIBM with multiple IBM corrections. Moreover, the L_2-norm error will be reduced significantly as $N_{\mathrm{IBM}} = 20$ and shows no obvious difference with larger values of N_{IBM}. Hence $N_{\mathrm{IBM}} = 20$ can provide a balance between accuracy and efficiency, and we will set $N_{\mathrm{IBM}} = 20$ in the following simulations.

Subsequently, two different resolution grids are used to discuss the performance overhead of the present KIBM, and the results are tabulated in Table I. The solver is run in serial mode on our Dell T7910 workstation, and the wall-clock time of DUGKS and IBM for 1000 steps is recorded after the flow attains steady state. The ratio of IBM to DUGKS is also provided in Table I. The performance is mainly influenced by the number of Eulerian grids, the number of Lagrangian grids, and IBM corrections times N_{IBM}. For the same grid, the time cost of every IBM correction is nearly identical,

TABLE II. Grid-independent study for flow over a stationary cylinder at Re = 20.

	Present			Cai *et al.* [21]		Tao *et al.* [53]		Linnick and Fasel [66]	
No.	Minimum grid sizes	C_d	L_w/D	C_d	L_w/D	C_d	L_w/D	C_d	L_w/D
Grid 1	$\Delta x = D/25$	2.176	1.03	2.101	0.995	2.13	0.95	2.16	0.93
Grid 2	$\Delta x = D/40$	2.161	1.02						
Grid 3	$\Delta x = D/50$	2.154	0.986						
Grid 4	$\Delta x = D/80$	2.147	0.971						
Grid 5	$\Delta x = D/160$	2.143	0.968						

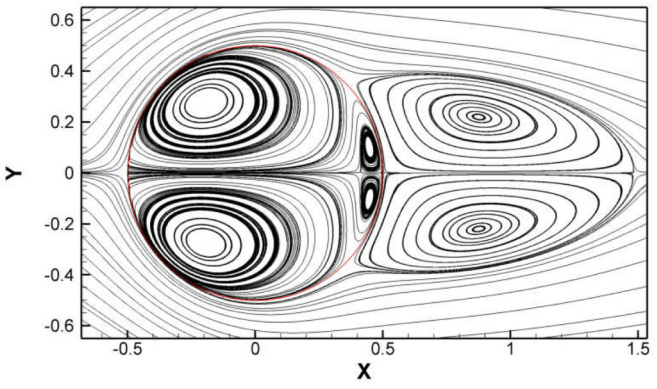

(a) Global view

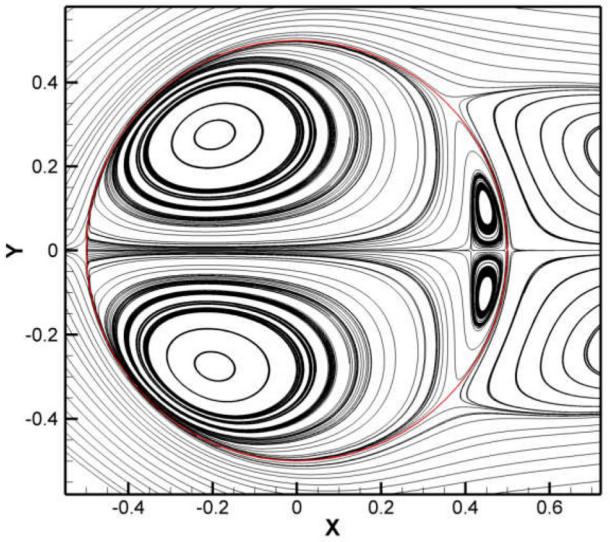

(b) Zoom-in view around the cylinder

FIG. 6. Streamlines for 2D flow around a stationary circular cylinder at Re = 20.

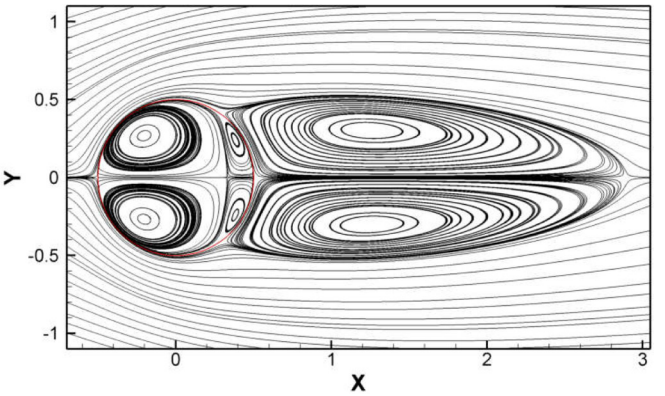

(a) Global view

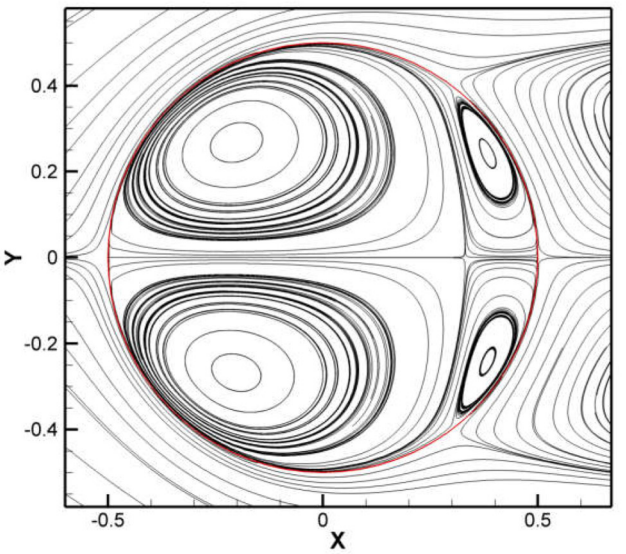

(b) Zoom-in view around the cylinder

FIG. 7. Streamlines for 2D flow around a stationary circular cylinder at Re = 40.

so the time cost of IBM is directly proportional to N_{IBM}. Based on the idea of nonequilibrium extrapolation, Tao *et al.* [56] developed another IBM combined with DUGKS, and we implemented Tao's IBM in our code to simulate the same flow for comparison. It is found that the performance overhead of the present KIBM is equivalent to Tao's IBM, so the present KIBM has an acceptable performance.

Finally, a grid-independent study has been performed at Re = 20 with multiple different spatial resolutions. The quantitative results of this flow are the ratio of recirculation length to the cylinder diameter L_w/D, and the drag coefficient $C_d = 2F_d/(\rho U_\infty^2 D)$, where F_d is the drag force acting on the immersed body. The obtained results by the present KIBM with five different resolution grids are tabulated in Table II, including the data available in the literature [21,53,66] for comparison, which shows that a minimum grid size $\Delta x = D/80$ seems to be good enough for this flow simulation, and the present KIBM has good agreement with the reference results.

In Fig. 6, the streamlines of the steady flow at Re = 20 (Grid 5: $\Delta x = D/160$) are presented, and a pair of symmetric recirculation bubbles appears behind the cylinder. In the zoomed-in view of the streamlines [Fig. 6(b)], there are no unphysical streamlines across the boundary of the cylinder, and the internal virtual fluid is visible without pulling out of the cylinder boundary. Hence, the no-slip and no-penetration boundary conditions can be exactly satisfied on the cylinder wall by the present KIBM. Similar results for the steady flow at Re = 40 are illustrated in Fig. 7. It is found that the streamlines inside and outside of the cylinder perfectly fit the boundary.

C. Horizontally oscillating circular cylinder in a stationary fluid

In order to validate the ability of the present KIBM to handle the fluid flows with a prescribed moving boundary, the flow induced by a horizontally oscillating circular cylinder in a stationary fluid is numerically simulated by the present KIBM. The numerical and experimental results of this problem have been reported in many studies [45,53,67]. In this problem, the governing dimensionless parameters are the Reynolds number $\mathrm{Re} = U_{\max} D/\nu$ and Keulegan-Carpenter number $\mathrm{KC} = U_{\max} T/D$. Here $U_{\max}$ is the amplitude of the

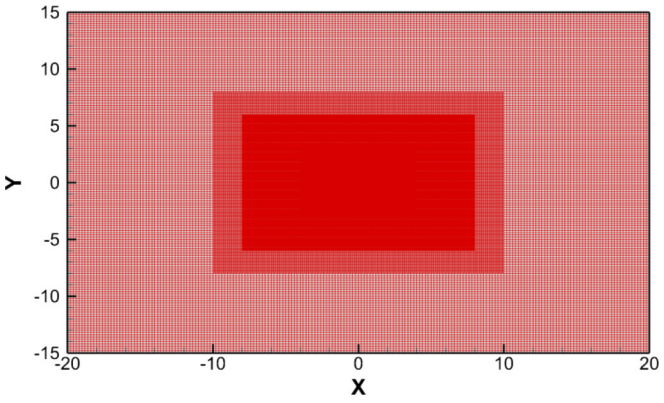

(a) Global view of grid

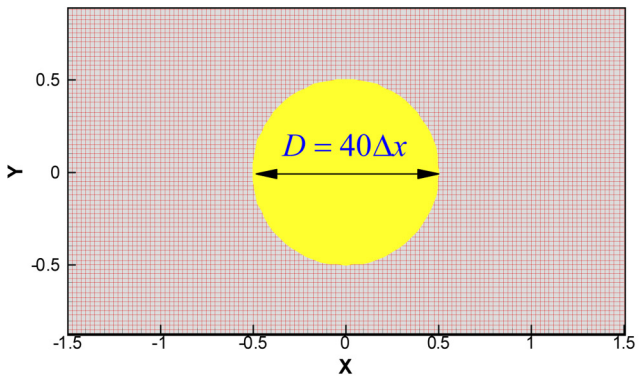

(b) Zoom-in view around the cylinder

FIG. 8. Nonuniform grid for horizontally oscillating circular cylinder in a stationary fluid.

oscillation velocity, D is the cylinder diameter, ν is the kinematic viscosity, and T is the period of oscillation. The cylinder is initialized at the center of the computational domain and oscillates with the following prescribed velocity:

$$\mathbf{U}_c(t) = \left[-U_{\max}\cos\left(\frac{2\pi t}{T}\right), 0\right]. \tag{46}$$

In the simulation, we set Re = 100, KC = 5, and CFL = 0.5. The computational domain is set by a square domain ($L \times W = 40D \times 30D$) with a nonuniform grid size of 169 200, which is shown in Fig. 8. There is a uniform region of size ($8D \times 6D$) around the cylinder, and the minimum grid spacing is $\Delta x = D/40$. Two hundred Lagrangian points are uniformly distributed along the cylinder surface, so the ratio of the Lagrangian grid size to the Eulerian grid size $\Delta S_L/\Delta x$ is about 0.63. Because the computational domain is large enough, the nonequilibrium extrapolation method is used for all boundaries.

The time variation of the drag coefficient $C_d = 2F_x/(\rho U_{\max}^2 D)$ is shown in Fig. 9, and the present results have good agreement with other diffusive interface IB-LBM [45] and experimental results [67]. It is noted that the experimental data provided by Dütsch *et al.* [67] are for periods after initial transient flows, so the first periods ($0 < t < T$) of the present results are cut off for comparison with Dütsch's data. In Fig. 10, the present velocity profiles of the horizontally

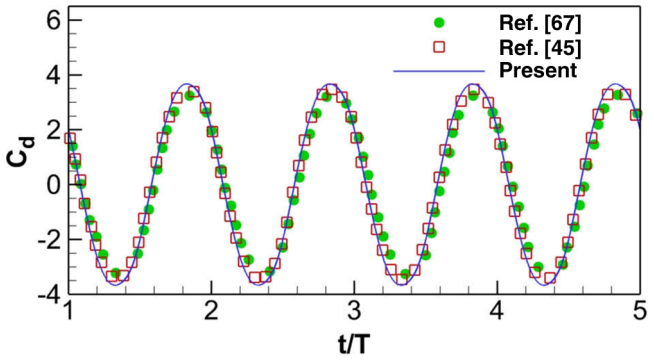

FIG. 9. Time variation of the drag coefficient $C_d = 2F_x/(\rho U_{\max}^2 D)$ of a horizontally oscillating circular cylinder in a stationary fluid for Re = 100 and KC = 5.

oscillating circular cylinder for Re = 100 and KC = 5 at four different locations $x = -0.6D$, 0.0, $0.6D$, and $1.2D$ for three different phase angles $\phi = (a)\,180^\circ$, $(b)\,210^\circ$, $(c)\,330^\circ$ are compared with the experimental results of Dütsch *et al.* [67], where the phase angle ϕ is defined as $\phi = t/T \times 360^\circ$. It is found that the present results are in agreement with Dütsch's results. In order to validate the satisfaction of no-slip and no-penetration boundary conditions, Fig. 11 shows the instantaneous streamlines of the flow in a relative reference frame fixed to the oscillating cylinder at four different times (a) $t = kT$, (b) $t = (k + 0.25)T$, (c) $t = (k + 0.5)T$, and (d) $t = (k + 0.75)T$, where k is a natural number. This flow with Re = 100 and KC = 5 is symmetric with respect to the x axis. At time $t = kT$ or $t = (k + 0.5)T$, the center of the cylinder locates at $x = 0$, and a pair of symmetric vortices develops before or behind the cylinder. The streamlines in Figs. 11(a) and 11(c) are similar to the flow around the stationary cylinder at low Re number. At time $t = (k + 0.25)T$ or $t = (k + 0.75)T$, the center of the cylinder arrives at the maximum displacement from equilibrium, and the vortices detach from the cylinder surface in Figs. 11(b) and 11(d). It is found that the streamlines obtained by the present KIBM do not penetrate the cylinder wall. It means that the no-slip and no-penetration boundary conditions on the oscillating cylinder wall are satisfied well by the present KIBM.

D. Sedimentation of a single elliptical particle under gravity in a closed narrow domain filled with fluid

Different from the prescribed movement of the body in Sec. IV C, in this case the sedimentation process of a free elliptical particle under gravity in a closed narrow domain filled with fluid is considered to further validate the reliability of the present KIBM to numerically simulate the flow interacting with a freely moving body. Moreover, compared with the cylindrical particle, the elliptical particle is anisotropic in shape and the flow mechanism is more complex, so it can more rigorously verify the present KIBM. This problem has been extensively studied by many researchers [45,53,68,69]. A schematic diagram of this problem is shown in Fig. 12. Two coordinate systems are introduced for this problem. One is the laboratory coordinate system, which is denoted as $o{-}X - Y$. Another is the body-fixed coordinate system $o' - X' - Y'$,

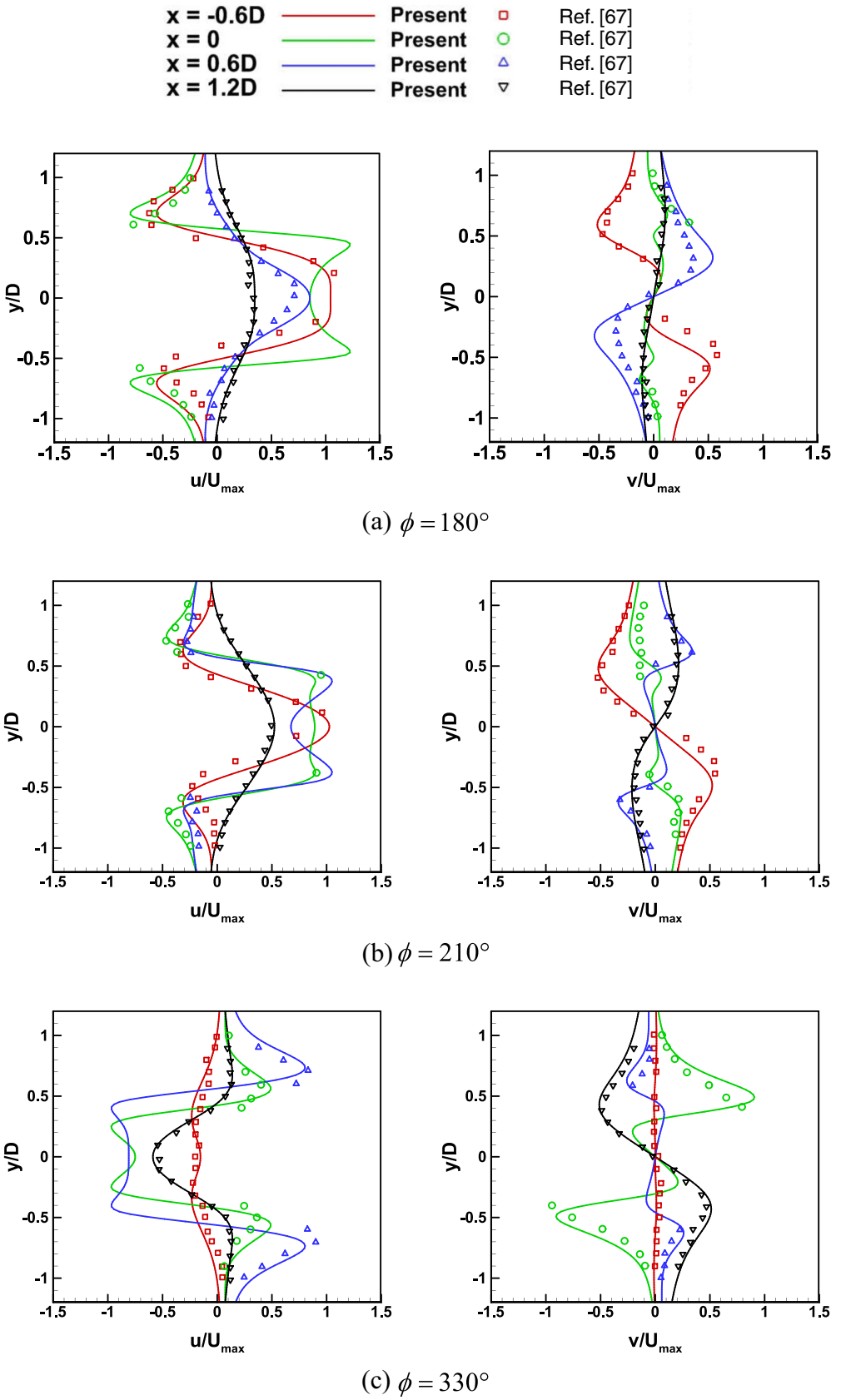

(a) $\phi = 180°$

(b) $\phi = 210°$

(c) $\phi = 330°$

FIG. 10. Velocity profiles of the flow around an oscillating cylinder at four different locations for three different phase angles.

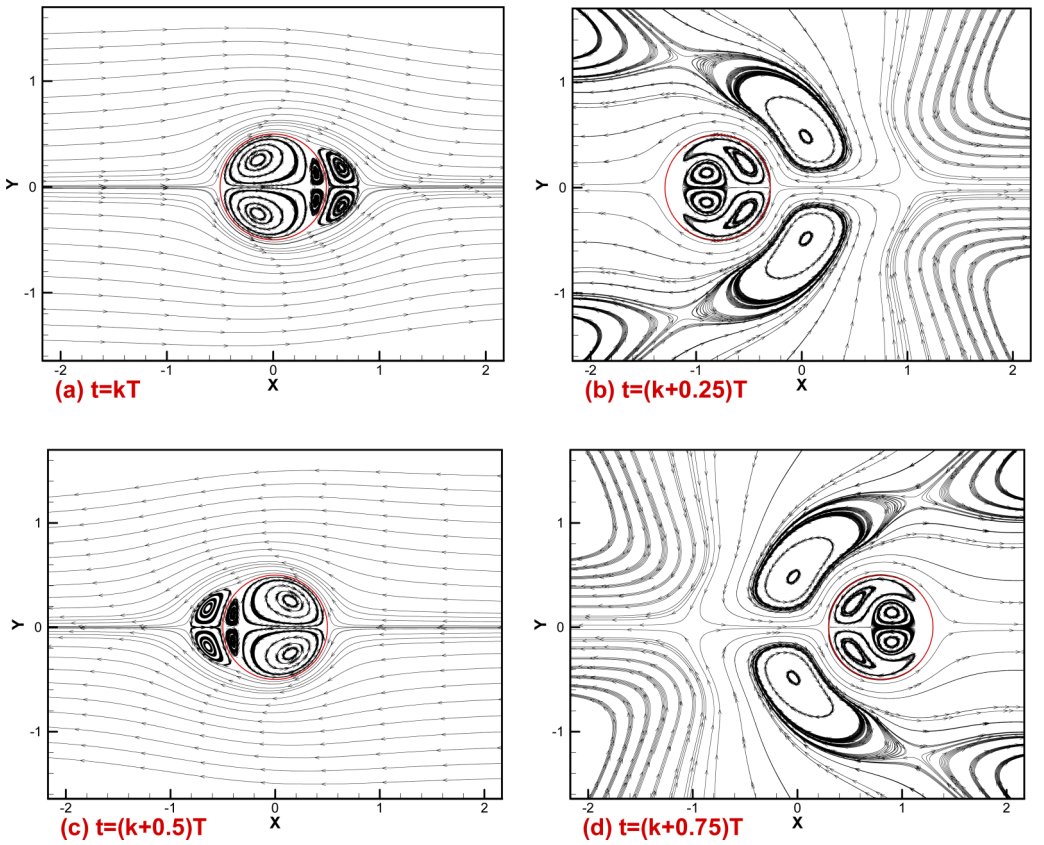

FIG. 11. Instantaneous streamlines of the flow in a relative reference frame fixed to the oscillating cylinder for Re = 100 and KC = 5 at four different times: (a) $t = kT$, (b) $t = (k + 0.25)T$, (c) $t = (k + 0.5)T$, and (d) $t = (k + 0.75)T$ (red circle is the cylinder wall).

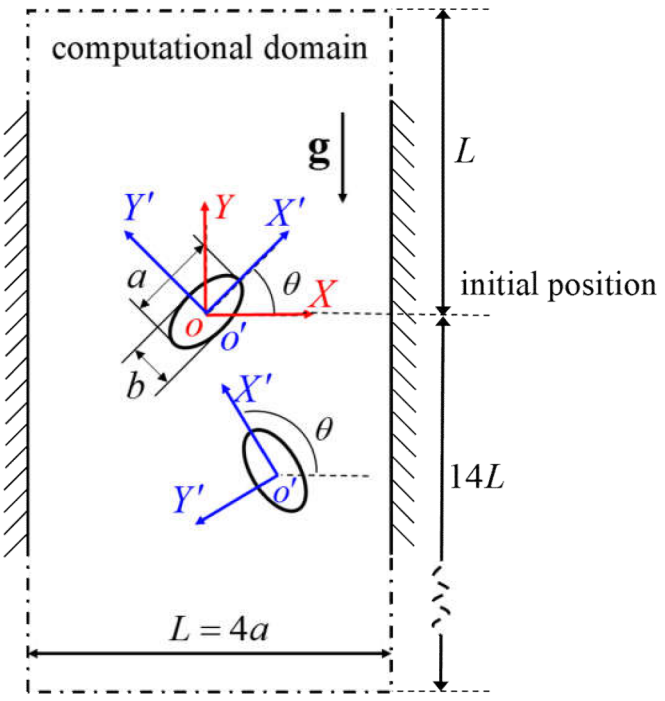

FIG. 12. Sedimentation of a single elliptical particle driven by a constant gravity acceleration in a closed narrow domain filled with fluid. The laboratory coordinate system is denoted as $o{-}X - Y$, and the body-fixed coordinate system as $o' - X' - Y'$. The rotational angle θ represents the angle between the axis X' and the axis X.

where the axes X' and Y' always coincide with the major and minor axes of the elliptical particle, respectively.

The major and minor axes of the elliptical particle are denoted as a and b, respectively, and the shape of the particle can be determined by the aspect ratio $\alpha = a/b$. The channel is placed vertically and the width of channel L is chosen as a length scale. The height of the computational domain is $15L$. The densities of fluid and particle are ρ_f and ρ_b, respectively. The acceleration of gravity is **g** along the negative Y direction. The governing dimensionless parameters of this problem are set as follows:

$$\begin{aligned} \text{Aspect ratio} \quad & \alpha = a/b = 2, \\ \text{Blockage ratio} \quad & \beta = L/a = 4, \\ \text{Density ratio} \quad & \rho_b/\rho_f = 1.1, \\ \text{Reynolds number} \quad & \mathrm{Re} = U_t L/\nu = 12.6, \end{aligned} \tag{47}$$

where ν is the kinematic viscosity and U_t is the terminal velocity of the particle. It is noted that U_t is determined by the density ratio ρ_b/ρ_f and the gravity acceleration **g**.

In this simulation, CFL = 0.5 and the computational domain is $L \times 15L$ with a uniform grid (200×3000), that is, $L = 200\Delta x$, where Δx is the grid spacing. One hundred fifty-one Lagrangian points are uniformly distributed along the elliptical particle surface. The elliptical particle is initialized at the origin of the laboratory coordinate system $(X, Y) = (0, 0)$ with the initial rotational angle $\theta = \pi/4$. Here, θ represents the angle between the axis X' of the body-fixed coordinate

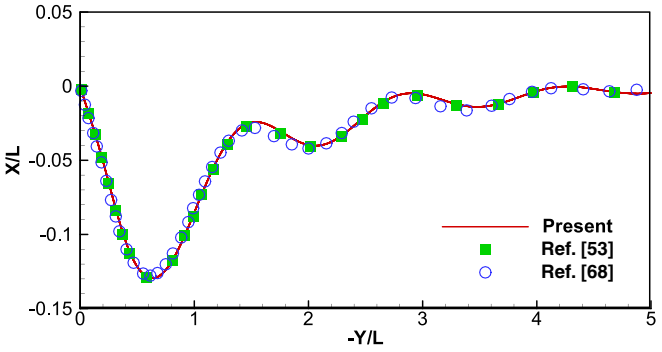

(a) Horizontal position of the center of the elliptical particle

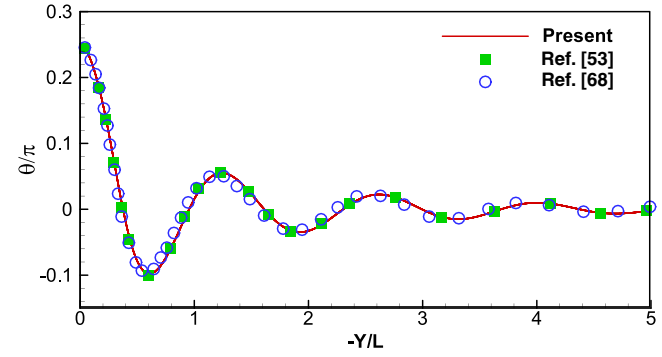

(b) Orientation of the elliptical particle

FIG. 13. Trajectory and orientation of an elliptical particle falling under gravity in a closed narrow domain filled with fluid.

system and the axis X of the laboratory coordinate system. It should be noted that the force acting on the elliptical particle has two parts, namely, $\mathbf{F}(t)$ in Eq. (37), and the buoyancy $G = (\rho_b - \rho_f)V_b\mathbf{g}$, where V_b is the volume of particle. The space motion of a rigid particle can be divided into two parts: a translation of the center of mass and a rotation around the center of mass, which are described by the Newton-Euler equations [53]. The bounce-back rule is imposed for the channel walls, and the nonequilibrium extrapolation method is applied for the top and bottom boundaries.

Figure 13 compares the trajectory of the particle mass center and the rotational angle with those in the literature. The results obtained by the present KIBM are in good agreement with the results by Xia *et al.* [68] and the diffusive interface IBM reported by Tao *et al.* [53]. For this case, the elliptical particle moves toward the centerline of the channel and approaches a steady sedimentation with the rotational angle $\theta \to 0$, which is consistent with the phenomenon reported in the literature [68].

Instantaneous streamlines at different time are plotted in Figs. 14(a)–14(c) under the laboratory coordinate system $o{-}X-Y$. It is clear that the elliptical particle pushes the surrounding fluid aside as it is falling under the gravity. The corresponding streamlines under the body-fixed coordinate system $o'-X'-Y'$ are drawn in Figs. 14(d)–14(f), which vividly illustrates the process of growth of the attached vortices behind the particle. Moreover, Fig. 15 displays the streamlines under the body-fixed coordinate system as the particle moves to $(Xc/L, Yc/L) = (6.2 \times 10^{-4}, -7.0)$. As expected, two attached vortices almost with the same size appear behind the particle. It is found that the streamlines obtained by the present KIBM do not penetrate the particle wall. It means that there is no mass exchange between the fluid outside the particle and the virtual fluid inside the particle.

V. DISCUSSION

All the above results have shown that the present KIBM has good agreement with other numerical and experimental results. The most remarkable feature of the present KIBM is that the general IB force density $G_L(\mathbf{X}, t)$ is expressed by the PDF discontinuity across the IB in Eq. (8), which is independent of any specific boundary conditions and any specific solvers of the Boltzmann equation. Hence, it can establish a unified framework for various types of boundary conditions to be incorporated into it. Meanwhile, it can be conveniently combined with any solvers of the Boltzmann equation, such as LBM, DUGKS, and other discrete ordinate methods.

As every coin has two sides, because the PDF is directly exchanged between the Lagrangian and Eulerian grids, the present KIBM is more expensive than the traditional IBMs based on the macroscopic flow variables. However, according to the performance overhead test shown in Sec. IV B, the present KIBM has an acceptable performance.

Just as mentioned in Sec. III B, the present KIBM is categorized into the diffusive interface IBM, because Peskin's isotropic regularized delta function is used in this paper. Then the boundary has an effective thickness, which is similar to other traditional diffusive interface IBMs [45,70]. Here the laminar flow past a flat plate is numerically simulated by the present KIBM to investigate the influence of the effective thickness of the boundary on the velocity profile. In this problem, a uniform flow with horizontal velocity $U_0 = 0.1$ flows past a flat plate with the length $L = 100$. The computational domain, shown in Fig. 16, is set to be $-L < x < 3L$ and $-L < y < L$ with the coordinate origin at the leading edge of the plate. The flow is characterized by the Reynolds number defined as $\mathrm{Re}_L = U_0 L/\nu$, where ν is the kinematic viscosity. In order to verify the stability of the present KIBM to simulate the boundary layer flow at higher Re numbers, we set $\mathrm{Re}_L = 2 \times 10^4$, which is 10 times as large as that in the article by Suzuki *et al.* [70]. Meanwhile, three different resolution nonuniform grids (301×111, 529×145, and 977×209) are chosen to obtain a grid-independent solution. The region near the flat plate adopts a refined uniform grid with different spacings $\Delta x = L/160$, $\Delta x = L/320$, and $\Delta x = L/640$; these are consistent with those of Suzuki *et al.* [70]. Single-layer Lagrangian elements with 160, 320, and 640 Lagrangian points, respectively, are uniformly distributed along the flat plate surface for the above three grids, so the ratio of the Lagrangian grid size to the Eulerian grid size is $\Delta S/\Delta x = 1$. Figure 17 shows the horizontal and vertical velocity profiles at the middle point of the plate, where the local Reynolds number is $\mathrm{Re}_x = U_0 x/\nu = 10^4$. Because the present KIBM is a diffusive interface IBM, so the immersed boundary has an effective thickness although the plate has no thickness in itself. It is similar to other diffusive interface IBMs [70]. When we set the effective thickness of boundary $h \approx 2\Delta x$ and shift

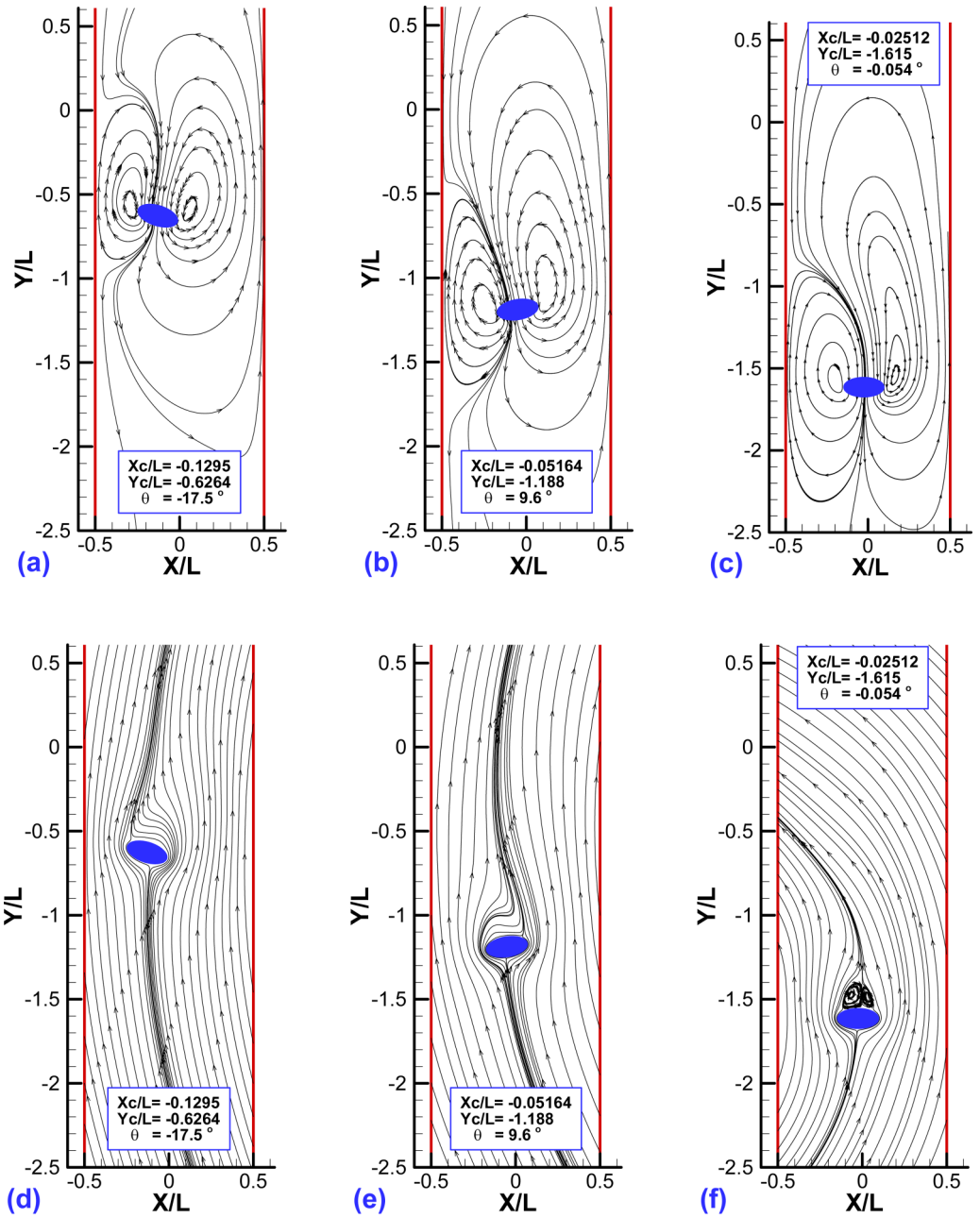

FIG. 14. Instantaneous streamlines of an elliptical particle falling under gravity in a closed narrow domain filled with fluid. (a)–(c) are plotted under the laboratory coordinate system $o-X-Y$, and (d)–(f) are drawn under the body-fixed coordinate system $o'-X'-Y'$.

the velocity profiles by $0.5h$ in the y direction, the results of the KIBM agree well with Howarth's [71] numerical solution of the Blasius equation, which is clearly shown in Figs. 17(b) and 17(c). In the article by Suzuki *et al.* [70], the boundary layer is well resolved by about 50 grids at $\mathrm{Re}_L = 2 \times 10^3$. This grid requirement for boundary layer capture at higher Re numbers will become unbearable. However, as displayed in Fig. 17(b), the present KIBM uses about eight to ten grids to well resolve the boundary layer at $\mathrm{Re}_L = 2 \times 10^4$, which is 10 times as large as that one in the article by Suzuki *et al.* Moreover, the present KIBM can provide stable and reasonable velocity profiles even with only five to six grids to resolve the boundary layer, which is shown in Fig. 17(a).

Finally, the present KIBM is categorized into the diffusive interface IBM, but the deduction of the general IB force density $G_L(\mathbf{X}, t) = [\![f]\!]\mathbf{u} \cdot \mathbf{n}$ is independent of any specific manner for obtaining the desired f_+ and f_- on both sides of the IB. Hence, the sharp interface IBM can also be developed under this framework if a one-sided kernel function is used instead of Peskin's isotropic regularized delta function. Just recently, Bale *et al.* [72] proposed a one-sided direct forcing IBM using moving least squares, so we will attempt to combine $G_L(\mathbf{X}, t) = [\![f]\!]\mathbf{u} \cdot \mathbf{n}$ with their one-sided kernel function to develop a sharp interface KIBM in the following work.

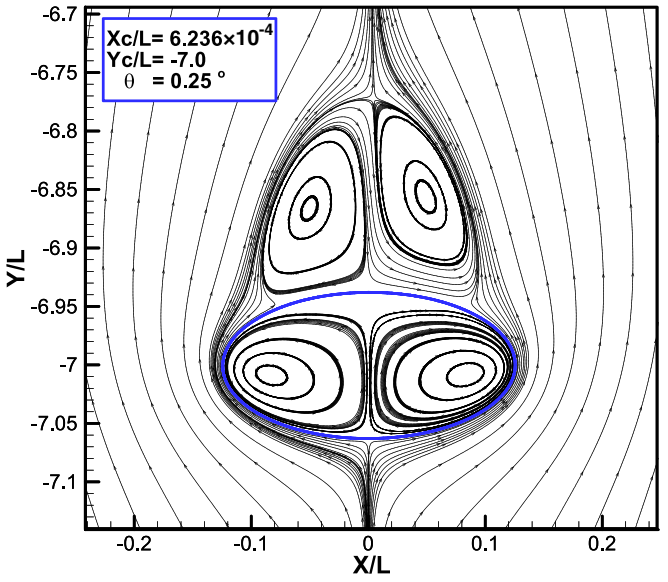

FIG. 15. Instantaneous streamlines drawn under the body-fixed coordinate system $o' - X' - Y'$. Two attached vortices with almost the same size appear behind the particle now.

VI. CONCLUSION

In this paper, the fluid-solid interface is denoted as a set of the Lagrangian marker points which are independent of the background Eulerian grids for fluid flow. The general IB force density $G_L(\mathbf{X}, t)$ is introduced on these Lagrangian marker points to represent the fluid-solid interaction on the boundary, and the formula of $G_L(\mathbf{X}, t)$ is directly deduced from the Boltzmann equation and finally expressed as the desired PDF discontinuity across the IB. Due to its independence of any specific boundary conditions and any specific solvers of the Boltzmann equation, it provides a possibility for incorporating various types of boundary conditions and several different kinds of solvers for the Boltzmann equation into a unified framework.

Subsequently, we propose the particle distribution function discontinuity-based kinetic immersed boundary method (KIBM) based on the general IB force density, and numerically implement it for the isothermal incompressible

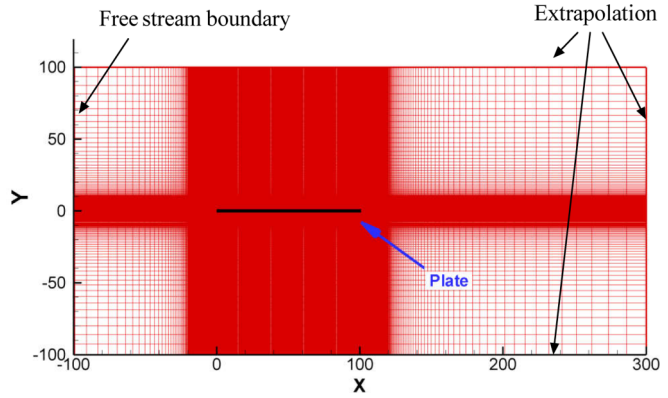

FIG. 16. Computational domain and nonuniform grid for the laminar flow over a flat plate ($\mathrm{Re}_L = 2 \times 10^4$).

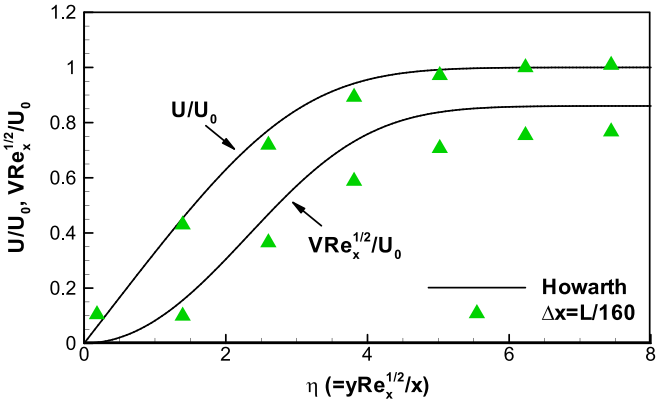

(a) Δx=L/160

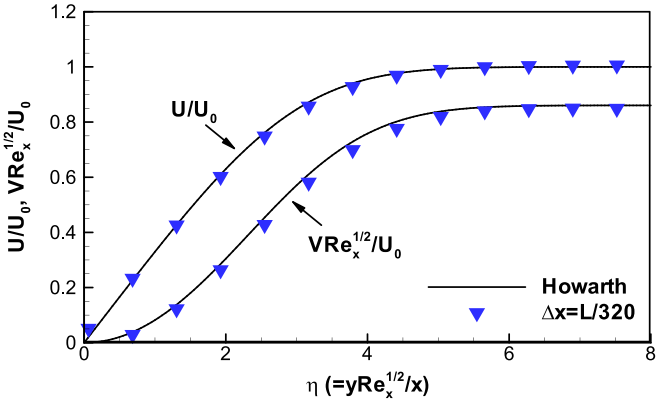

(b) Δx=L/320

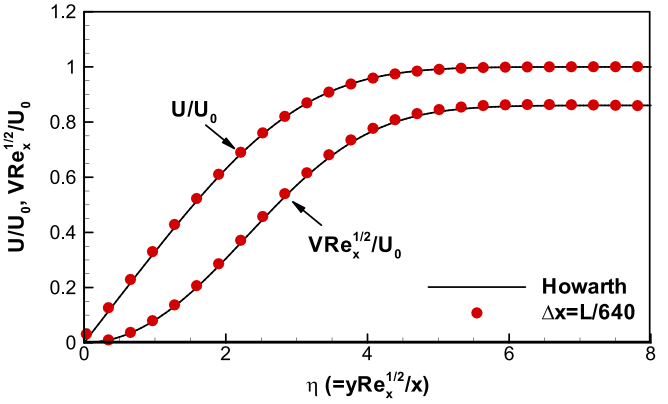

(c) Δx=L/640

FIG. 17. Horizontal and vertical velocity profiles of the flat plate boundary layer at the middle point of the plate where local $\mathrm{Re}_x = 10^4$. Three different resolution grids (a) $\Delta x = L/160$, (b) $\Delta x = L/320$, and (c) $\Delta x = L/640$ are used by the present KIBM to obtain a grid-independent solution, which is compared with Howarth's [71] numerical solution of the Blasius equation.

fluid-solid flows. The discrete unified gas kinetic scheme (DUGKS) is used to solve the Boltzmann-BGK model equation because of its flexibility and stability, and Peskin's isotropic regularized delta function is adopted for

exchanging information between the Lagrangian and Eulerian grids. Meanwhile, the bounce-back rule combined with the iterative IBM correction procedure is employed in enforcing the no-penetration and no-slip boundary conditions on the solid wall. Several typical benchmark problems including stationary body, prescribed moving body, and freely moving body flows have been carried out to investigate the accuracy, performance, and reliability of the present KIBM. The comparison of our results with references showed the good capability of the present KIBM to simulate isothermal incompressible fluid-solid flows in complex geometries.

Although only two-dimensional flows are numerically simulated by the present KIBM in this paper, this KIBM can actually be applied to three-dimensional flows without any theoretical restrictions. For future work, the application of the present KIBM to three-dimensional problems will be performed. Meanwhile, the present KIBM in this paper is targeted toward isothermal incompressible fluid-solid flows in complex geometries, and further development of KIBM for the thermal compressible flows remains a goal for our future work.

ACKNOWLEDGMENTS

This work is supported by National Numerical Wind Tunnel Project (Grant No. NNW2019ZT3-A14) and the NSFC (National Natural Science Foundation of China) under Contract No.11102150.

[1] C. S. Peskin, J. Comput. Phys. **25**, 220 (1977).
[2] R. Mittal and G. Iaccarino, Annu. Rev. Fluid Mech. **37**, 239 (2005).
[3] J. H. Seo and R. Mittal, J. Comput. Phys. **230**, 7347 (2011).
[4] H. Luo, H. Dai, P. J. S. A. Ferreira de Sousa *et al.*, Comput. Fluids **56**, 61 (2012).
[5] J. Boustani, M. F. Barad, C. C. Kiris *et al.*, J. Comput. Phys. **438**, 110369 (2021).
[6] J. Kim, D. Kim, and H. Choi, J. Comput. Phys. **171**, 132 (2001).
[7] X. Zhang, X. Gu, and N. Ma, Comput. Fluids **220**, 104871 (2021).
[8] F. Sotiropoulos and X. Yang, Prog. Aerosp. Sci. **65**, 1 (2014).
[9] W.-X. Huang, C. B. Chang, and H. J. Sung, J. Comput. Phys. **230**, 5061 (2011).
[10] Y. Kim and C. S. Peskin, Phys. Fluids **19**, 053103 (2007).
[11] W.-X. Huang, C. B. Chang, and H. J. Sung, J. Comput. Phys. **231**, 3340 (2012).
[12] E. A. Fadlun, R. Verzicco, P. Orlandi *et al.*, J. Comput. Phys. **161**, 35 (2000).
[13] M. Uhlmann, J. Comput. Phys. **209**, 448 (2005).
[14] K. Luo, Z. Wang, J. Fan, and K. Cen, Phys. Rev. E **76**, 066709 (2007).
[15] J. Wu and C. Shu, J. Comput. Phys. **228**, 1963 (2009).
[16] X. Wang, C. Shu, J. Wu *et al.*, Comput. Fluids **100**, 165 (2014).
[17] Y. Hu, H. Yuan, S. Shu *et al.*, Comput. Math. Appl. **68**, 140 (2014).
[18] M. Jiang and Z. Liu, J. Comput. Phys. **390**, 203 (2019).
[19] S. Tschisgale, T. Kempe, and J. Fröhlich, Comput. Fluids **170**, 285 (2018).
[20] A. Pinelli, I. Z. Naqavi, U. Piomelli *et al.*, J. Comput. Phys. **229**, 9073 (2010).
[21] Y. Cai, S. Li, and J. Lu, Int. J. Numer. Methods Fluids **87**, 109 (2018).
[22] C. S. Peskin, Acta Numer. **11**, 479 (2002).
[23] G. Iaccarino and R. Verzicco, Appl. Mech. Rev. **56**, 331 (2003).
[24] W.-X. Huang and F.-B. Tian, Proc. Inst. Mech. Eng., Part C **233**, 7617 (2019).
[25] B. E. Griffith and N. A. Patankar, Annu. Rev. Fluid Mech. **52**, 421 (2020).
[26] Y. H. Qian, D. D'Humières, and P. Lallemand, Europhys. Lett. **17**, 479 (1992).
[27] X. Y. He and L. S. Luo, Phys. Rev. E **56**, 6811 (1997).
[28] S. Chen and G. D. Doolen, Annu. Rev. Fluid Mech. **30**, 329 (2003).
[29] K. Xu and K. H. Prendergast, J. Comput. Phys. **114**, 9 (1994).
[30] K. Xu, J. Comput. Phys. **171**, 289 (2001).
[31] K. Xu and J. C. Huang, J. Comput. Phys. **229**, 7747 (2010).
[32] K. Xu and C. Liu, Phys. Fluids **29**, 026101 (2017).
[33] Z. L. Guo, K. Xu, and R. J. Wang, Phys. Rev. E **88**, 033305 (2013).
[34] L. H. Zhu, Z. L. Guo, and K. Xu, Comput. Fluids **127**, 211 (2016).
[35] D. Z. Yu, R. W. Mei, L. S. Luo *et al.*, Prog. Aerosp. Sci. **39**, 329 (2003).
[36] C. K. Aidun and J. R. Clausen, Annu. Rev. Fluid Mech. **42**, 439 (2009).
[37] M. Righi, Flow, Turbul. Combust. **97**, 121 (2016).
[38] L. Tang, Comput. Fluids **56**, 39 (2012).
[39] O. J. Chit, A. A. Omar, W. Asrar *et al.*, AIAA J. **43**, 1427 (2005).
[40] C. Liu, K. Xu, Q. Sun *et al.*, J. Comput. Phys. **314**, 305 (2016).
[41] L. H. Zhu and Z. L. Guo, Phys. Rev. E **95**, 023113 (2017).
[42] Z.-G. Feng and E. E. Michaelides, J. Comput. Phys. **195**, 602 (2004).
[43] X. D. Niu, C. Shu, Y. T. Chew *et al.*, Phys. Lett. A **354**, 173 (2006).
[44] S. K. Kang and Y. A. Hassan, Int. J. Numer. Methods Fluids **66**, 1132 (2011).
[45] K. Suzuki and T. Inamuro, Comput. Fluids **49**, 173 (2011).
[46] S. Tao, Q. He, J. Chen *et al.*, Appl. Math. Modell. **76**, 362 (2019).
[47] C. S. Peskin and B. F. Printz, J. Comput. Phys. **105**, 33 (1993).
[48] M.-C. Lai and Z. Li, Appl. Math. Lett. **14**, 149 (2001).
[49] K. Suzuki and M. Yoshino, Comput. Fluids **172**, 593 (2018).
[50] K. Suzuki, K. Ishizaki, and M. Yoshino, Phys. Fluids **33**, 047104 (2021).
[51] R. Yuan, C. Zhong, and H. Zhang, J. Comput. Phys. **296**, 184 (2015).
[52] R. Yuan and C. Zhong, Appl. Math. Modell. **55**, 417 (2018).
[53] S. Tao, H. Zhang, Z. Guo *et al.*, J. Comput. Phys. **375**, 498 (2018).

[54] S. Tao, Q. He, L. Wang *et al.*, Int. J. Heat Mass Transfer **137**, 476 (2019).
[55] C. Li and L.-P. Wang, Int. J. Heat Mass Transfer **126**, 1059 (2018).
[56] S. Tao, B. Chen, X. Yang *et al.*, Comput. Fluids **165**, 54 (2018).
[57] B. Caswell, Arch. Ration. Mech. Anal. **26**, 385 (1967).
[58] L. H. Zhu, P. Wang, and Z. L. Guo, J. Comput. Phys. **333**, 227 (2017).
[59] A. J. C. Ladd, J. Fluid Mech. **271**, 311 (1994).
[60] S. Tschisgale, T. Kempe, and J. Fröhlich, J. Comput. Phys. **339**, 432 (2017).
[61] Z.-G. Feng and E. E. Michaelides, Comput. Fluids **38**, 370 (2009).
[62] Z. L. Guo, C. G. Zheng, and S. B. Chang, Chin. Phys. B **11**, 366 (2002).
[63] P. Wang, S. Tao, and Z. Guo, Comput. Fluids **120**, 70 (2015).
[64] Y. Cheng, L. Zhu, and C. Zhang, Commun. Comput. Phys. **16**, 136 (2014).
[65] K. Suzuki and T. Inamuro, Comput. Fluids **76**, 105 (2013).
[66] M. N. Linnick and H. F. Fasel, J. Comput. Phys. **204**, 157 (2005).
[67] H. Dütsch, F. Durst, S. Becker *et al.*, J. Fluid Mech. **360**, 249 (1998).
[68] Z. Xia, K. W. Connington, S. Rapaka *et al.*, J. Fluid Mech. **625**, 249 (2009).
[69] Y. Chen, Q. Cai, Z. Xia, M. Wang, and S. Chen, Phys. Rev. E **88**, 013303 (2013).
[70] K. Suzuki, I. Okada, and M. Yoshino, J. Fluid Sci. Technol. **11**, JFST0017 (2016).
[71] L. Howarth, Proc. R. Soc. London, Ser. A **164**, 547 (1938).
[72] R. Bale, A. P. S. Bhalla, B. E. Griffith *et al.*, J. Comput. Phys. **440**, 110359 (2021).